Research Article Vol. 56, No. 35 / December 10 2017 / Applied Optics 9779

applied optics

Wide-angle absorption of visible light from simple bilayers

Athanasios N. Papadimopoulos,[1] Nikolaos V. Kantartzis,[1] Nikolaos L. Tsitsas,[2] and Constantinos A. Valagiannopoulos[3,*]

[1]Department of Electrical and Computer Engineering, Aristotle University of Thessaloniki, 54124 Thessaloniki, Greece
[2]Department of Informatics, Aristotle University of Thessaloniki, Thessaloniki GR-54124, Greece
[3]Department of Physics, School of Science and Technology, Nazarbayev University, 53 Qabanbay Batyr Ave, Astana, KZ-010000, Kazakhstan
*Corresponding author: konstantinos.valagiannopoulos@nu.edu.kz

Received 8 August 2017; revised 19 October 2017; accepted 12 November 2017; posted 13 November 2017 (Doc. ID 304219); published 8 December 2017

Color-selective absorption of light is a very significant operation used in numerous applications, from photonic sensing and switching to optical signal modulation and energy harnessing. We demonstrate angle-insensitive and polarization-independent absorption by thin bilayers comprising ordinary bulk media: dielectrics, semiconductors, and metals. Several highly efficient designs for each color of the visible spectrum are reported, and their internal fields' distributions reveal the resonance mechanism of absorption. The proposed bilayer components are realizable, since various physical or chemical deposition methods can be used for their effective fabrication. The absorption process is found to exhibit endurance with respect to the longitudinal dimension of the planar structure, which means that the same designs could be successfully utilized in non-planar configurations composed of arbitrary shapes.

OCIS codes: (160.1245) Artificially engineered materials; (160.3918) Metamaterials; (310.5448) Polarization, other optical properties; (310.6628) Subwavelength structures, nanostructures.

https://doi.org/10.1364/AO.56.009779

1. INTRODUCTION

Absorption of electromagnetic waves is a fundamental operation, extensively employed in a large assortment of photonic and electronic devices. The effective collection of incoming illumination and its conversion to other energy types constitutes a basic operational step in every structure processing the power of the signals or manipulating their optical features. Except the obvious application to photovoltaic cells, which harvest the solar energy and convert it into thermal form [1], sensing individual quantum objects and estimating the percentage of impurities into solutions [2] are also based on the use of media that control the absorption. Moreover, thermal emission (blackbody effect) and directional emissivity are phenomena directly related to perfect absorption, which can lead to efficient designs of frequency-selective light-emitting diodes and polarization-tuning gratings [3].

The basic techniques adopted in the modeling and design of effective absorbers follow one universal principle: achieving a balanced regime between electric and magnetic response (resonance) which guarantees zero reflection, with suitable losses that ensure negligible transmission [4]. In particular, one can achieve high absorption via a Huygens sheet formed by induced electric and magnetic surface currents [5,6]. Similarly, symmetric absorbers are devised by balancing effective electric and magnetic resistive sheets [7–10], whereas unilateral structures are obtained by depositing resonant particles or layers on lossy bases [11–19]. However, such designs usually require costly and complex fabrication processes, which hinder their practical applicability. In contrast, planar layered thin films are much more easily constructed, while they reportedly [20,21] attain selective high absorption in the visible spectrum.

In this work, we propose a simple absorber for the visible light by using a bilayer configuration: two optically thin slabs, one deposited onto the other. Such a structure, despite its minimalistic nature, is extensively utilized to describe various effects, such as tunneling in epsilon-near-zero layers [22] and phase transition in parity-time symmetric slabs [23]. It is the simplest model that can capture the interaction between two adjacent components. This setup is employed also for the cases of atomic lattices, such as bilayers of transition metal dichalcogenides [24] or catalytically active metals and oxides [25]. The featured bilayer consists of a common semiconductor, playing the role of the capacitor, and an ordinary lossy metal corresponding to the inductor of the equivalent resonance circuit. We examine a great variety of combinations of the materials composing the two layers and choose their thicknesses

by maximizing a metric that takes into account all the angles of incident light. In this manner, we select those frequencies for which the regarded structures absorb equally well both polarizations of the incoming illumination and populate a table with numerous efficient designs for each color of visible light. The metric used to rate our structures concerns the energy that escapes from it, regardless of the direction; so, wide-angle absorption can be reported. Consequently, we provide many alternative realizations to achieve high absorption with the structural advantage of the thin size, which can mildly change the shape at will, without being restricted by bulk metallic bases. Numerical simulations demonstrate the efficiency of the phenomenon, even for bilayers of finite length.

Harmonic time dependence of the form $e^{+i2\pi ft}$, where f is the operational frequency, t denotes time, and $i=\sqrt{-1}$, is assumed and suppressed throughout the subsequent analysis.

2. ANALYSIS

A. Configuration and Objective

We consider the simple structure of two thin adjacent slabs with thicknesses h_1 and h_2, respectively [Fig. 1(a), where the Cartesian coordinate system (x, y, z) is also defined]. The two slab regions are filled with materials of relative and frequency dispersive complex permittivities $\varepsilon_1=\varepsilon_1(f)$ and $\varepsilon_2=\varepsilon_2(f)$, respectively. The whole structure is placed into vacuum, characterized by ε_0 and μ_0. The bilayer is excited by all possible incidence angles $(0<\theta<\pi/2)$ (within propagating spectrum) and polarizations (TE/TM).

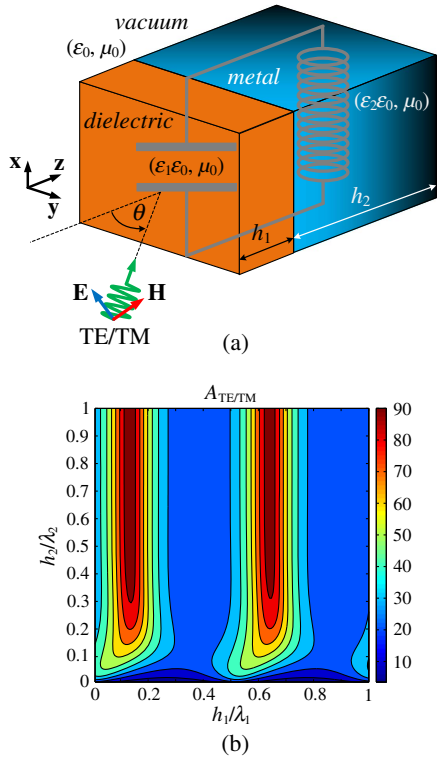

Fig. 1. (a) Configuration of the proposed structure: a thin resonant bilayer absorbs maximally (by suitably selecting its parameters) an arbitrary incident plane wave. (b) Variation of the absorption metric A_{TE} (percent results) of Eq. (2) on the electrical thicknesses map $(h_1/\lambda_1, h_2/\lambda_2)$ for the gallium phosphide–platinum combination.

After considering the field expansions in the different domains of the problem and imposing the transmission boundary conditions on the planar interfaces, we find that the reflection and transmission coefficients can be determined by means of the 2×2 linear systems (TE/TM):

$$\begin{bmatrix} 1+\frac{pu_2}{qu_1} & 1-\frac{pu_2}{qu_1} \\ 1-\frac{pu_2}{qu_1} & 1+\frac{pu_2}{qu_1} \end{bmatrix} \cdot \begin{bmatrix} \frac{u_2+q\cos\theta}{u_2} e^{+ik_0h_2(u_2-\cos\theta)} \\ \frac{u_2-q\cos\theta}{u_2} e^{-ik_0h_2(u_2+\cos\theta)} \end{bmatrix} T_{TE/TM} = 2\begin{bmatrix} \frac{u_1-p\cos\theta}{u_1} e^{-ik_0h_1(u_1+\cos\theta)} \\ \frac{u_1+p\cos\theta}{u_1} e^{+ik_0h_1(u_1-\cos\theta)} \end{bmatrix} R_{TE/TM} + 2\begin{bmatrix} \frac{u_1+p\cos\theta}{u_1} e^{-ik_0h_1(u_1-\cos\theta)} \\ \frac{u_1-p\cos\theta}{u_1} e^{+ik_0h_1(u_1+\cos\theta)} \end{bmatrix}, \quad (1)$$

with $u_j=\sqrt{\varepsilon_j-\sin^2\theta}$ (for $j=1, 2$), $k_0=2\pi/\lambda_0$ the vacuum wavenumber, λ_0 the vacuum wavelength, while $(p, q)=(1, 1)$ for TE polarization and $(p, q)=(\varepsilon_1, \varepsilon_2)$ for TM polarization.

A metric of how effectively the featured structure absorbs the incident illumination can be expressed as

$$A_{TE/TM}=\int_0^{\pi/2}(1-|R_{TE/TM}|^2-|T_{TE/TM}|^2)\cos\theta d\theta. \quad (2)$$

Note that factor $\cos\theta$ in the integrand of Eq. (2) is used to take into account only the longitudinal direction of the power flow (regardless of the incidence angle); indeed, the transverse spatial distribution is dictated by the incident field excitation, and the related variations (along y direction) are the same for each of the considered regions of our problem. For example, it is well known that the reflection coefficient at the grazing angle ($\theta=90°$) takes unitary value, i.e., $\lim_{\theta\to\pi/2}|R_{TE/TM}(\theta)|=1$, regardless of the texture of the reflecting plane. Therefore, absorption for this angle is inevitably zero for all proposed simple designs. With the considered metric of (2), such a contribution is not taken into account, and the actual absorption rate of the device is fairly evaluated. The same metric has been used in [26] to characterize the performance of a parity-time symmetric absorber. It is stressed that the presence of $\cos\theta$ in Eq. (2), which magnifies the contribution from the close-to-normal incidence rays against the one from close-to-grazing angles ($\theta\to 90°$), makes the responses for the two polarizations (TE/TM) to look similar. Hence, we do not anticipate obtaining extreme differences between absorption metrics A_{TE} and A_{TM} for the same design. Mainly, our aim is to find combinations of actual materials, which, for suitable thicknesses, exhibit substantial A_{TE} and A_{TM}, when illuminated by visible light.

B. Physical Justifications

Our quest for well-performing designs contains numerous materials, including bulk metals, semiconductors, and inorganic dielectrics, whose permittivity profiles are obtained from the well-established material database [27] containing data from highly cited references, such as [28–30]. In the following, we assume that the dielectric permittivities ε_1 and ε_2 of our

media (measured for thin samples) remain the same at a specific frequency f, regardless of their thicknesses. Furthermore, we focus on thin films with a thickness of less than the effective wavelength in each material, namely, $0 < h_j < \lambda_j$ (for $j = 1, 2$), where $\lambda_j = 1/(f\sqrt{\varepsilon_0\mu_0|\varepsilon_j|}) = \lambda_0/\sqrt{|\varepsilon_j|}$. The considered frequency range covers the entire visible spectrum (red, orange, yellow, green, blue, and violet color), i.e., 400 THz $< f <$ 800 THz. The medium that first meets the incident field is chosen to be either dielectric ($\mathrm{Im}[\varepsilon_1] = 0$) or semiconducting ($\mathrm{Im}[\varepsilon_1] \neq 0$), with $\mathrm{Re}[\varepsilon_1] > 0$, since the use of (hugely mismatched) metals, instead, would cause strong reflection, harming thus the absorbing operation of the device. In this way, the first layer plays the role of a "mediator" between vacuum, with which it is coarsely matched, and the second layer, where the attenuation takes place. Hence, the second layer should be metallic ($\mathrm{Re}[\varepsilon_2] < 0$) in order to resonate with the first one and maximize the absorbed energy. Actually, the absorption mechanism, as schematically depicted in Fig. 1(a), corresponds to a lossy LC circuit working at resonance. Under normal incidence, the dielectric ($\mathrm{Re}[\varepsilon_1] > 1$) slab behaves for $h_1 \ll \lambda_1$ like a capacitor [31] with capacitance $C = \varepsilon_0 h_1 \frac{(\mathrm{Re}[\varepsilon_1]-1)^2+(\mathrm{Im}[\varepsilon_1])^2}{\mathrm{Re}[\varepsilon_1]-1}$ of internal conductance $g_1 = 2\pi f \varepsilon_0 h_1 \frac{(\mathrm{Re}[\varepsilon_1]-1)^2+(\mathrm{Im}[\varepsilon_1])^2}{|\mathrm{Im}[\varepsilon_1]|}$, and the metallic ($\mathrm{Re}[\varepsilon_2] < 0$) slab acts for $h_2 \ll \lambda_2$ as an inductor with inductance $L = \frac{1-\mathrm{Re}[\varepsilon_2]}{(2\pi f)^2\varepsilon_0 h_2\{(1-\mathrm{Re}[\varepsilon_2])^2+(\mathrm{Im}[\varepsilon_2])^2\}}$ of internal conductance $g_2 = 2\pi f \varepsilon_0 h_2 \frac{(\mathrm{Re}[\varepsilon_2]-1)^2+(\mathrm{Im}[\varepsilon_2])^2}{|\mathrm{Im}[\varepsilon_2]|}$ [32,33]. Note that $\mathrm{Im}[\varepsilon_1], \mathrm{Im}[\varepsilon_2] < 0$ for the considered harmonic time convention. Additionally, owing to the definition of the absorption metric given in Eq. (2), we can evaluate the performance of the configuration regardless of the incidence angle θ.

For a specific combination of media and frequency, the typical variations of both metrics A_{TE} and A_{TM} bear strong similarities to each other on the $(h_1/\lambda_1, h_2/\lambda_2)$ map and are analogous to the one presented in Fig. 1(b). Two zones of high absorption are recorded along a single wavelength λ_1 of the dielectric medium. The first one, appearing at the lower h_1, is attributed to the aforesaid resonance of the equivalent LC circuit [17]. On the other hand, the second zone in the vicinity of a larger h_1 appears due to the periodicity of fields into the almost lossless λ_1-periodic first layer; apparently, the squared field magnitudes (associated with $A_{\mathrm{TE/TM}}$) repeat their patterns every $\lambda_1/2$. As far as the second layer is concerned, its size has evidently a beneficial effect on $A_{\mathrm{TE/TM}}$, because of the significant losses exhibited by metals in the visible spectrum. However, too thick metallic slabs are not necessary, as the incremental absorption gain becomes smaller for an increasing h_2. Indeed, after reaching a critical h_2 threshold, the selection of a larger thickness achieves only a smaller (than the already negligible) transmission, whereas the reflection remains untouched. This is why we select h_2 close to that threshold [indicated by the dark red region of the representative variation in Fig. 1(b)] and h_1 equal to the value that maximizes the represented metrics.

C. Designing and Fabrication Processes

The previous procedure of selecting the best (h_1, h_2) pair is repeated for numerous frequencies, scanning the optical spectrum, and every single combination between the inorganic dielectrics and metallic films, whose permittivities are available via measurements and fitting models [27]. As a consequence, we obtain the best absorption rate that a pair of two specific media can achieve as a function of the frequency f of visible light. In this manner, we determine a range of frequencies that our bilayer exhibits very high absorption for both the considered polarizations (TE/TM). As implied above, the (h_1, h_2) pair that offers very high A_{TE} usually works for the TM polarization, as well (i.e., attaining a very high A_{TM}).

An informative set of results is summarized in the Table 1, where we examine the best combinations among those provided by the extensive material database in [27], between dielectrics/semiconductors (rows) and metals (columns). Moreover, in this table, each color of the visible light (blank box means that significant absorption is not observed) is associated with the frequency at which the respective bilayer [for a specific (h_1, h_2) pair] absorbs maximally both incident polarizations (TE/TM). In most cases, the corresponding metrics for the proposed designs attain very high values: $A_{\mathrm{TE}}, A_{\mathrm{TM}} > 93\%$ and exhibit also significant tolerance with respect to changes in the operating frequency (wideband behavior). It should be emphasized that a specific pair of materials does not work only at the indicated frequency; for an alternative selection of h_1 and h_2, a high performance can be reached at other bands as well. With reference to Fig. 1(b), Table 1 includes designs corresponding either to the first (lower h_1) or the second (higher h_1) resonance zone in order to provide multiple alternatives in experimental realizations. Finally, by inspecting Table 1, one can draw useful conclusions about the frequencies that certain media combinations prefer to absorb. For instance, GaSb and InSb favor absorption of red light, while GaAs and Si change the frequency band of operation with respect to which metallic substrate is placed below them.

The highly performing designs indicated in Table 1, where one thin dielectric layer is deposited on a metallic foil, are in most cases realistic structures that can be fabricated. Recent advances in the thin film industry and technology have allowed the construction of layers of materials in the range of a few nanometers [34,35], thus rendering realizable all these tiny bilayers. The practice of applying a thin film onto a surface is called thin-film deposition [36], where the surface might be a substrate or another previously deposited layer. A variation of the well-known electroplating process, called electrochemical deposition, enables the construction of remarkably thin metallic layers onto semiconducting surfaces [37,38]. Ultra-thin semiconducting films can also be made through spin coating [39]. Furthermore, the chemical vapor deposition (CVD) [40] and atomic layer deposition (ALD) techniques [41,42] are processes that produce thin films of excellent quality and uniformity for a broad range of materials. Molecular beam epitaxy (MBE) is a renowned, notably precise but rather costly deposition technique [43,44]. Moreover, sputtering [45], where particles are ejected from a solid target material as it is bombarded by energetic particles, is widely used in the industry for the deposition of metals [46]. Finally, the pulsed layer deposition (PLD) has been given account for being able to construct thin metal films [47]. It involves a pulsed laser

Table 1. Frequencies (Indicated Also by the Corresponding Color of the Visible Spectrum) and Material Thicknesses for Each Combination of the Available Materials at Which the Proposed Bilayer of Fig. 1(a) Absorbs Maximally (with $A_{TE/TM} > 93\%$) the Incident Field[a]

	Aluminum (Al)	Copper (Cu)	Gold (Au)	Platinum (Pt)	Silver (Ag)	Titanium (Ti)
Aluminium Antimonide (AlSb)	610 THz $h_1 = 15$ nm $h_2 = 36$ nm	570 THz $h_1 = 10$ nm $h_2 = 92$ nm	600 THz $h_1 = 7$ nm $h_2 = 98$ nm	500 THz $h_1 = 21$ nm $h_2 = 60$ nm	650 THz $h_1 = 8$ nm $h_2 = 95$ nm	520 THz $h_1 = 15$ nm $h_2 = 95$ nm
Carbon (C)		660 THz $h_1 = 25$ nm $h_2 = 72$ nm	780 THz $h_1 = 21$ nm $h_2 = 67$ nm	750 THz $h_1 = 26$ nm $h_2 = 75$ nm		720 THz $h_1 = 24$ nm $h_2 = 76$ nm
Gallium Arsenide (GaAs)	430 THz $h_1 = 128$ nm $h_2 = 30$ nm	580 THz $h_1 = 11$ nm $h_2 = 84$ nm	490 THz $h_1 = 97$ nm $h_2 = 83$ nm	410 THz $h_1 = 31$ nm $h_2 = 60$ nm	690 THz $h_1 = 6$ nm $h_2 = 77$ nm	410 THz $h_1 = 27$ nm $h_2 = 94$ nm
Gallium Phosphide (GaP)	730 THz $h_1 = 65$ nm $h_2 = 42$ nm	710 THz $h_1 = 9$ nm $h_2 = 82$ nm	640 THz $h_1 = 73$ nm $h_2 = 112$ nm	620 THz $h_1 = 16$ nm $h_2 = 60$ nm	740 THz $h_1 = 57$ nm $h_2 = 82$ nm	530 THz $h_1 = 20$ nm $h_2 = 81$ nm
Gallium Antimonide (GaSb)	410 THz $h_1 = 28$ nm $h_2 = 39$ nm	440 THz $h_1 = 17$ nm $h_2 = 75$ nm	450 THz $h_1 = 14$ nm $h_2 = 78$ nm		440 THz $h_1 = 17$ nm $h_2 = 75$ nm	
Germanium (Ge)	450 THz $h_1 = 21$ nm $h_2 = 41$ nm	480 THz $h_1 = 10$ nm $h_2 = 84$ nm	490 THz $h_1 = 9$ nm $h_2 = 95$ nm		480 THz $h_1 = 11$ nm $h_2 = 79$ nm	
Indium Arsenide (InAs)	400 THz $h_1 = 38$ nm $h_2 = 37$ nm	490 THz $h_1 = 18$ nm $h_2 = 89$ nm	510 THz $h_1 = 15$ nm $h_2 = 95$ nm	400 THz $h_1 = 31$ nm $h_2 = 62$ nm	510 THz $h_1 = 17$ nm $h_2 = 77$ nm	
Indium Phosphide (InP)	600 THz $h_1 = 21$ nm $h_2 = 34$ nm	560 THz $h_1 = 15$ nm $h_2 = 92$ nm	580 THz $h_1 = 11$ nm $h_2 = 98$ nm	400 THz $h_1 = 38$ nm $h_2 = 63$ nm	640 THz $h_1 = 12$ nm $h_2 = 90$ nm	430 THz $h_1 = 27$ nm $h_2 = 90$ nm
Indium Antimonide (InSb)		410 THz $h_1 = 18$ nm $h_2 = 81$ nm	400 THz $h_1 = 19$ nm $h_2 = 79$ nm		400 THz $h_1 = 22$ nm $h_2 = 91$ nm	
Silicon (Si)	700 THz $h_1 = 55$ nm $h_2 = 40$ nm	620 THz $h_1 = 9$ nm $h_2 = 96$ nm	630 THz $h_1 = 7$ nm $h_2 = 99$ nm	440 THz $h_1 = 28$ nm $h_2 = 63$ nm	730 THz $h_1 = 44$ nm $h_2 = 84$ nm	550 THz $h_1 = 14$ nm $h_2 = 91$ nm

[a]Every design refers to different thicknesses for the two layers, while blank (shaded) boxes correspond to poor absorption performance.

beam that strikes a target material, vaporizes, and deposits it into thin layers under ultra-high vacuum conditions.

3. NUMERICAL RESULTS

A. Frequency Responses and Field Profiles

The effectiveness of the featured bilayers is demonstrated in Figs. 2(a) and 2(b), where the absorption of six of the highly efficient bilayers as a function of the operational frequency is showcased. Specifically, for each of the six basic colors of the visible light, we pick a pair of materials, based on Table 1, and project their absorption along a broad (around 200 THz) range of the optical spectrum. Then, for every combination of these media (given in the caption of Fig. 2), the thicknesses that achieve maximum absorption are selected according to Table 1, and the A_{TE} and A_{TM} metrics are accordingly computed. As detected, for both the TE and TM polarizations, all bilayers attain an exceptional wide-angle absorption: in most cases both A_{TE} and A_{TM} exceed the level of 93%. Observe that the frequency ranges of notable absorption may vary significantly from one material combination to another and can be quite wideband, as in the InAs–Ag pair, or considerably more frequency selective, as in the Si–Ag counterpart (where its response changes abruptly, operating like a switch). It is also worth mentioning that, although all bilayer thicknesses follow the designs for the specified frequencies of Table 1, even greater absorption can be accomplished at frequencies neighboring to the designated ones.

Next, we examine the spatial field profiles of various bilayer configurations. To this aim, Fig. 3(a) considers a normally incident illumination and depicts the square magnitude of the sole total electric field component, $|E_y|^2$, along the z axis. The results concern both polarizations, since for $\theta = 0°$ a TE plane wave is only trivially different from the TM one. Three configuration setups are considered: (i) an optimized bilayer consisting of GaP and Au with fixed thicknesses of $h_1 = 73$ nm and $h_2 = 112$ nm, as indicated in Table 1, operating at $f = 640$ THz, (ii) a single metallic layer made of Au with the same h_2 thickness, and (iii) a bilayer where both thicknesses h_1, h_2, and the metallic layer (composed of Au) are kept unaltered, while the best dielectric for these specified thicknesses is replaced by GaAs. As expected, the reflected electric field is fairly small for the optimized bilayer, because high levels of absorption imply low levels of reflection. On the contrary, reflections are notably higher for the single metallic layer due to the negative real part of the dielectric permittivity ($\mathrm{Re}[\varepsilon_2] < 0$), which causes a huge impedance mismatch at the interface. However, the obtained reflections from the third bilayer are not in

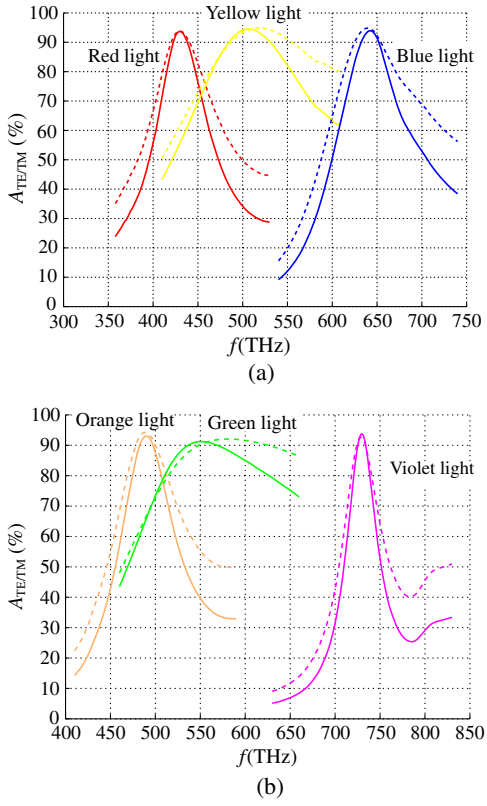

Fig. 2. Absorption metrics A_{TE} (solid lines) and A_{TM} (dashed lines) versus operational frequency for six highly efficient designs of absorbing bilayers, working at the (a) red (GaAs with Al), yellow (InAs with Ag), and blue (GaP with Au) and (b) orange (GaAs with Au), green (InP with Cu), and violet (Si with Ag) colors of the visible spectrum.

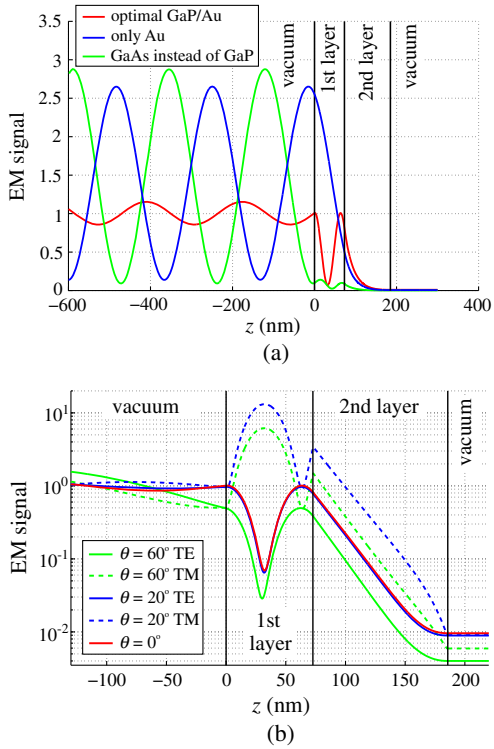

Fig. 3. (a) Variation of $|E_y|^2$ along the z axis for an optimized bilayer (red line), a single metallic layer (blue line), and a suboptimal bilayer (green line). The angle of incidence is $\theta = 0°$ and the operating frequency $f = 640$ THz. (b) Variation of $|E_y|^2$ (solid lines) and $\eta_0^2|H_y|^2$ (dashed lines) along the z axis for the optimized (GaP–Au) bilayer at the same frequency and various incidence angles.

between those of the two prior designs: the incident field perturbation is even stronger than case (ii) of a single Au layer. This emphasizes the importance of the data presented in Table 1, namely, high absorption is achieved only by picking the suitable combinations not only of materials but also of the corresponding layers' thicknesses. An arbitrarily selected dielectric–metal bilayer does not necessarily make an efficient absorber, yet rather the opposite. Note that for the best case, the electric field is almost entirely transmitted in magnitude through the dielectric nonetheless with a very different phase. The square magnitude of the total electric field is proportionate to the electromagnetic field's energy. Consequently, this phase shift is related to high levels of absorption of light by our bilayer, as it enables the metal to receive almost the entire incoming field's energy and attenuate it. It is also worth stating that we deliberately chose a design working at the second zone of high absorption, which requires thicker dielectric layers, so that field profiles in the different layers are more easily distinguishable.

Moreover, Fig. 3(b) illustrates quantities similar to Fig. 3(a) along the z axis for the case of oblique incidence and different polarizations, regarding the previously mentioned GaP–Au bilayer. In particular, for the TE polarization, we provide $|E_y|^2$, whereas for the TM polarization, the corresponding magnetic signal $\eta_0^2|H_y|^2$ ($\eta_0 = \sqrt{\mu_0/\varepsilon_0}$ is the wave impedance into vacuum), in order for the two quantities to be comparable. Apparently, more obliquely incident waves (larger θ) generate more substantial reflections, since our metrics emphasize the contribution from the normal incidence. It is, however, remarkable that a very high absorption is attained for small angles ($\theta = 20°$) in both polarizations; this feature demonstrates the tolerance of our design with respect to the angle θ. The phase in the total field magnitude oscillations (in the $z < 0$ vacuum space) is different in the TE and TM cases, when $\theta = 20°$, owing to the fact that different fields (E_y and H_y) are examined, which in the normal incidence are out of phase. For the same reason, the represented quantities are locally minimized into the dielectric layer for the TE polarization and maximized for the TM one.

B. Bilayers of Finite Length

In the previous analysis and numerical processing, only bilayers of infinite length have been considered. Herein, we use finite samples of our well-performing designs, making arbitrarily oriented shapes, and assess their absorbing efficiency against the incoming illumination. Thus, in Fig. 4(a), we approximately shape the "NU" logo with Pt flanges of thickness $h_2 = 60$ nm, which extend to several vacuum wavelengths λ_0. The structure is excited by orange light ($f = 500$ THz, where $\varepsilon_2 \cong -17.8 - i11$), in the form of four plane waves that

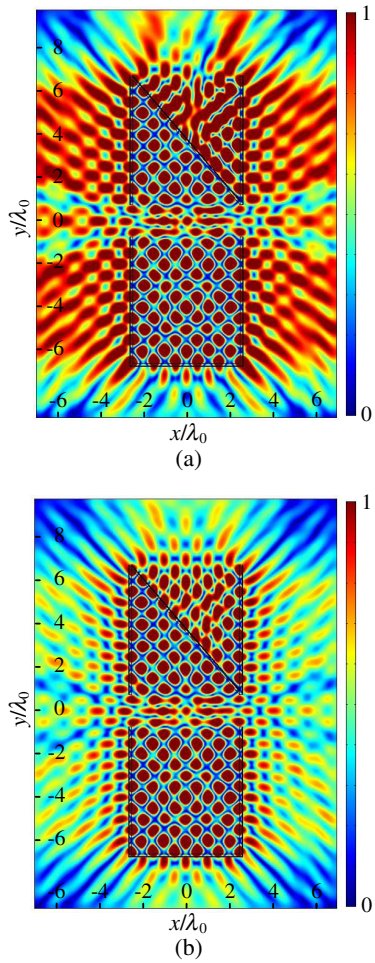

Fig. 4. Spatial distribution of the normalized scattered field magnitude by finitely long boundaries, forming an approximate schema of the "NU" logo and made of: (a) metallic films and (b) ultra-absorbing bilayers. The structure is illuminated by four plane waves imposed at the four sides of the external rectangular simulation box.

illuminate the complex boundary around the simulation box: $\mathbf{E}_{\text{inc}}(x,y) = \hat{\mathbf{z}}(e^{-ik_0x} + e^{+ik_0x} + e^{-ik_0y} + e^{+ik_0y})$. In this context, Fig. 4(a) presents the magnitude of the scattered electric field on the $(x/\lambda_0, y/\lambda_0)$ plane, normalized by its maximum value (computed via the commercial simulation software COMSOL Multiphysics [48]). It is stressed that we are not interested in the field distribution in the interior of the boundaries, where the total field is negligible, and hence the scattered field is almost opposite to the incident component $\mathbf{E}_{\text{inc}}$. What should be emphasized, however, are the strong reflections outside the complex boundary, due to the excessive mismatch between vacuum and the plasmonic Pt flanges.

On the other hand, Fig. 4(b) displays the same quantity, but boundaries are now made of the proposed ultra-efficient absorbing bilayer for $f = 500$ THz, as given in Table 1. Actually, the Pt film is externally covered by an AlSb ($\varepsilon_1 \cong 15.8 - i0.04$) layer with a thickness of $h_1 = 21$ nm. As expected, the internal field remains almost the same as that of Fig. 4(a), since the transmission from the bilayer is practically identical (and of very small magnitude) to that of the metal

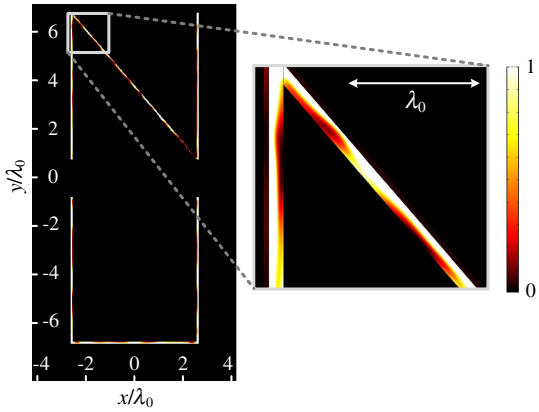

Fig. 5. Spatial distribution of the normalized absorbed power by finitely long, highly absorbing bilayers, forming an approximate schema of the "NU" logo. The excitation is identical to that of Fig. 4.

alone. On the contrary, the reflections from the "NU" boundaries are significantly mitigated due to the high absorption of the used bilayer. It should be mentioned that the finite length of the boundaries deteriorates their absorbing performance; however, the difference from the absorption by the metallic frame alone remains substantial. Therefore, we can conclude that the proposed structures work relatively well even when their lengths are not infinite, but comparable to the operating wavelength λ_0. Furthermore, the reflection from the skewed boundary of letter "N" is stronger, since the highly absorbing design under-emphasizes the contribution from oblique incidences. Nonetheless, and apart from the finite nature of the employed bilayers, the non-negligible reflections in Fig. 4(b) can be attributed to the refraction from the sharp metallic edges, which are absent in the case of infinite slabs.

Finally, Fig. 5 shows the spatial distribution of the normalized absorbed power for the case of Fig. 4(b), which has been proposed to maximally absorb waves with minimal reflection and transmission. Obviously, the higher values are recorded at the cross section of the metal (Pt), which is far more lossy than AlSb under orange light illumination; in this way, we have a clear sketch of the "NU" logo, indicating the high absorption region. In the inset, one may notice that maximum absorption is attained along the external surface of the structure, which is reasonable because the excitation wave comes from that side. Conversely, along the internal surface of the Pt layer, the field (and accordingly the absorbed power) follows a pattern with alternating low-absorption regions.

4. CONCLUSIONS

An efficient and straightforward-to-implement structure, comprised of two planar layers has been optimized with respect to electrically small dimensions and the available bulk media at optical frequencies in order to absorb the incident illumination. The employed absorption metric takes into account all the incidence angles of propagating waves and gets maximized for both polarizations. Both slabs, constituting the bilayer, are from materials with permittivities of opposite real part signs for the formulation

of an equivalent resonant circuit. Specifically, the dielectric/semiconducting layer plays the role of "mediator" between vacuum, with which it is coarsely matched, and the plasmonic/metallic layer is the one where the attenuation takes place. Various efficient designs are reported for all the visible colors, and their frequency responses demonstrate their selectivity and suitability to work as filters and switches. Moreover, the spatial distribution of the electromagnetic signal into the bilayer reveals the resonance mechanism via which the incident light is absorbed. The reflections remain quite low and the transmission negligible, even when the length of the structure is finite. As a consequence, the proposed designs, which are also realizable through an assortment of fabrication techniques, provide an extensive "toolbox" for assisting experimental works.

Funding. Alexander S. Onassis Public Benefit Foundation (GZL060-1/2015-2016).

Acknowledgment. The major part of this study was produced during the visit of Mr. A. N. Papadimopoulos to the School of Science and Technology of Nazarbayev University. The authors thank Dr. Olzat Toktarbaiuly and Dr. Ozhet Mauit for discussions on the experimental potential of the proposed design.

REFERENCES

1. H. A. Atwater and A. Polman, "Plasmonics for improved photovoltaic devices," Nat. Mater. **9**, 205–213 (2010).
2. N. Liu, M. Mesch, T. Weiss, M. Hentschel, and H. Giessen, "Infrared perfect absorber and its application as plasmonic sensor," Nano Lett. **10**, 2342–2348 (2010).
3. S. Collin, "Nanostructure arrays in free-space: optical properties and applications," Rep. Prog. Phys. **77**, 126402 (2014).
4. Y. Ra'di, C. R. Simovski, and S. A. Tretyakov, "Thin perfect absorbers for electromagnetic waves: theory, design, and realizations," Phys. Rev. Appl. **3**, 037001 (2015).
5. Y. Ra'di, V. S. Asadchy, and S. A. Tretyakov, "Total absorption of electromagnetic waves in ultimately thin layers," IEEE Trans. Antennas Propag. **61**, 4606–4614 (2013).
6. C. A. Valagiannopoulos and S. A. Tretyakov, "Symmetric absorbers realized as gratings of PEC cylinders covered by ordinary dielectrics," IEEE Trans. Antennas Propag. **62**, 5089–5098 (2014).
7. D. Pozar, "Scattered and absorbed powers in receiving antennas," IEEE Antennas Propag. Mag. **46**, 144–145 (2004).
8. W. Padilla and X. Liu, "Perfect electromagnetic absorbers from microwave to optical," in *Optical Design & Engineering* (SPIE Newsroom, 2010).
9. I. S. Nefedov, C. A. Valagiannopoulos, S. M. Hashemi, and E. I. Nefedov, "Total absorption in asymmetric hyperbolic media," Sci. Rep. **3**, 2662 (2013).
10. I. S. Nefedov, C. A. Valagiannopoulos, and L. A. Melnikov, "Perfect absorption in graphene multilayers," J. Opt. **15**, 114003 (2013).
11. N. I. Landy, S. Sajuyigbe, J. J. Mock, D. R. Smith, and W. J. Padilla, "Perfect metamaterial absorber," Phys. Rev. Lett. **100**, 207402 (2008).
12. Y. Q. Ye, Y. Jin, and S. He, "Omnidirectional, polarization-insensitive and broadband thin absorber in the terahertz regime," J. Opt. Soc. Am. B **27**, 498–504 (2010).
13. K. Aydin, V. E. Ferry, R. M. Briggs, and H. A. Atwater, "Broadband polarization-independent resonant light absorption using ultrathin plasmonic super absorbers," Nat. Commun. **2**, 517 (2011).
14. B. Zhang, J. Hendrickson, and J. Guo, "Multispectral near-perfect metamaterial absorbers using spatially multiplexed plasmon resonance metal square structures," J. Opt. Soc. Am. B **30**, 656–662 (2013).
15. H. Wang and L. P. Wang, "Perfect selective metamaterial solar absorbers," Opt. Express **21**, A1078–A1093 (2013).
16. T. Cao, L. Zhang, R. E. Simpson, and M. J. Cryan, "Mid-infrared tunable polarization-independent perfect absorber using a phase-change metamaterial," J. Opt. Soc. Am. B **30**, 1580–1585 (2013).
17. C. A. Valagiannopoulos, A. Tukiainen, T. Aho, T. Niemi, M. Guina, S. A. Tretyakov, and C. R. Simovski, "Perfect magnetic mirror and simple perfect absorber in the visible spectrum," Phys. Rev. B **91**, 115305 (2015).
18. W. Kim, B. S. Simpkins, J. P. Long, B. Zhang, J. Hendrickson, and J. Guo, "Localized and nonlocalized plasmon resonance enhanced light absorption in metal-insulator-metal nanostructures," J. Opt. Soc. Am. B **32**, 1686–1692 (2015).
19. R. Smaali, F. Omeis, A. Moreau, T. Taliercio, and E. Centeno, "A universal design to realize a tunable perfect absorber from infrared to microwaves," Sci. Rep. **6**, 32589 (2016).
20. M. A. Kats, R. Blanchard, G. Patrice, and F. Capasso, "Nanometre optical coatings based on strong interference effects in highly absorbing media," Nat. Mater. **12**, 20–24 (2013).
21. J. Liang, L. I. Hou, and J. Li, "Frequency tunable perfect absorber in visible and near-infrared regimes based on VO_2 phase transition using planar layered thin films," J. Opt. Soc. Am. B **33**, 1075–1080 (2016).
22. S. Savoia, G. Castaldi, V. Galdi, A. Alù, and N. Engheta, "Tunneling of obliquely incident waves through pt-symmetric epsilon-near-zero bilayers," Phys. Rev. B **89**, 085105 (2014).
23. R. Guo, L. Wu, X. Cao, and J. Chen, "Oblique-incidence-induced phase transition in parity-time symmetric optical bilayers," J. Opt. **18**, 025611 (2016).
24. M. Bernardi, M. Palummo, and J. C. Grossman, "Extraordinary sunlight absorption and one nanometer thick photovoltaics using two-dimensional monolayer materials," Nano Lett. **13**, 3664–3670 (2013).
25. M. S. Chen and D. W. Goodman, "The structure of catalytically active gold on titania," Science **306**, 252–255 (2004).
26. C. A. Valagiannopoulos, F. Monticone, and A. Alù, "PT-symmetric planar devices for field transformation and imaging," J. Opt. **18**, 044028 (2016).
27. RefractiveIndex.INFO, *Refractive Index Database* (2015).
28. D. E. Aspnes and A. A. Studna, "Dielectric functions and optical parameters of Si, Ge, GaP, GaAs, GaSb, InP, InAs, and InSb from 1.5 to 6.0 eV," Phys. Rev. B **27**, 985–1009 (1983).
29. G. E. Jellison, "Optical functions of silicon determined by two-channel polarization modulation ellipsometry," Opt. Mater. **1**, 41–47 (1992).
30. A. D. Rakić, A. B. Djurišić, J. M. Elazar, and M. L. Majewski, "Optical properties of metallic films for vertical-cavity optoelectronic devices," Appl. Opt. **37**, 5271–5283 (1998).
31. N. Engheta, "Circuits with light at nanoscales: optical nanocircuits inspired by metamaterials," Science **317**, 1698–1702 (2007).
32. S. Tretyakov, *Analytical Modeling in Applied Electromagnetics* (Artech House, 2003).
33. C. A. Valagiannopoulos and A. Sihvola, "Low-pass features of optical nano-filters constituted by simple layered structures," Microw. Opt. Technol. Lett. **55**, 2099–2106 (2013).
34. K. Seshan, *Handbook of Thin Film Deposition: Techniques, Processes, and Technologies*, 3rd ed. (Elsevier, 2012).
35. K. L. Chopra, P. D. Paulson, and V. Dutta, "Thin-film solar cells: an overview," Prog. Photovoltaics **12**, 69–92 (2004).
36. M. Ohring, *Materials Science of Thin Films*, 2nd ed. (Elsevier, 2001).
37. M. Paunovic and M. Schlesinger, *Fundamentals of Electrochemical Deposition*, 2nd ed. (Wiley, 2006).
38. G. Oskam, J. G. Long, A. Natarajan, and P. C. Searson, "Electrochemical deposition of metals onto silicon," J. Phys. D **31**, 1927–1949 (1998).
39. D. B. Mitzi, L. L. Kosbar, C. E. Murray, M. Copel, and A. Afzali, "High-mobility ultrathin semiconducting films prepared by spin coating," Nature **428**, 299–303 (2004).
40. J.-H. Park and T. S. Sudarshan, *Chemical Vapor Deposition* (ASM International, 2001).
41. S. M. George, "Atomic layer deposition: an overview," Chem. Rev. **110**, 111–131 (2010).
42. O. Sneh, R. B. Clark-Phelps, A. R. Londergan, J. Winkler, and T. E. Seidel, "Thin film atomic layer deposition equipment for semiconductor processing," Thin Solid Films **402**, 248–261 (2002).

43. B. A. Joyce, "Molecular beam epitaxy," Rep. Prog. Phys. **48**, 1637–1697 (1985).
44. A. Y. Cho, "Growth of III-V semiconductors by molecular beam epitaxy and their properties," Thin Solid Films **100**, 291–317 (1983).
45. P. Sigmund, "Theory of sputtering. I. Sputtering yield of amorphous and polycrystalline targets," Phys. Rev. **184**, 383–416 (1969).
46. O. Almén and G. Bruce, "Collection and sputtering experiments with noble gas ions," Nucl. Instrum. Methods **11**, 257–278 (1961).
47. J. G. Lunney, "Pulsed laser deposition of metal and metal multilayer films," Appl. Surf. Sci. **86**, 79–85 (1995).
48. COMSOL Inc., *COMSOL Multiphysics*® (2015).